

**EBNA1-targeted probe for the imaging and growth inhibition of tumours associated with
the Epstein-Barr virus**

Lijun Jiang¹, Rongfeng Lan¹, Tao Huang², Chi-Fai Chan³, Hongguang Li¹, Sam Lear⁴, Jingyi Zong⁴, Wing-Yan Wong³, Magnolia Muk-Lan Lee³, Brandon Dow Chan³, Wai-Lun Chan¹, Wai-Sum Lo³, Nai-Ki Mak^{5*}, Maria Li Lung⁶, Hong Lok Lung⁵, Sai Wah Tsao⁷, Graham S. Taylor⁸, Zhao-Xiang Bian², William C. S. Tai³, Ga-Lai Law^{3*}, Wing-Tak Wong^{3*}, Steven L. Cobb^{4*}, and
Ka-Leung Wong^{1*}

^a. Department of Chemistry, Hong Kong Baptist University, Kowloon Tong, Hong Kong SAR, China.

^b. Department of Biology, Hong Kong Baptist University, and Centre for Nasopharyngeal Carcinoma Research, University of Hong Kong, Hong Kong SAR.

^c. Clinical Division, School of Chinese Medicine, Hong Kong Baptist University, Kowloon Tong, Hong Kong SAR, China.

^d. Department of Chemistry, Durham University, Durham DH1 3LE, UK.

^e. State Key Laboratory of Chiroscience, Department of Applied Biological and Chemical Technology, Hong Kong Polytechnic University, Hung Hum, Hong Kong SAR, China.

^f. Department of Clinical Oncology, University of Hong Kong, and Cancer for Nasopharyngeal Carcinoma Research, University of Hong Kong, Hong Kong SAR;

^g. School of Biomedical Sciences, University of Hong Kong, Hong Kong SAR;

^h. School of Cancer Sciences, University of Birmingham, Vincent Drive, Birmingham, B15 2TT, United Kingdom.

Abstract

Epstein-Barr Nuclear Antigen 1 (EBNA1), a dimeric oncoprotein of the Epstein-Barr virus (EBV), is essential for both viral-genome maintenance and the survival of infected cells. Despite EBNA1's potential as a therapeutic target, tools for the direct monitoring of EBNA1 *in vitro* and *in vivo* are lacking. Here, we show that a peptide-based inhibitor that luminesces when bound to EBNA1 inside the nucleus of EBV+ cells can regulate EBNA1 homodimer formation and selectively inhibit the growth of EBV+ tumours of nasopharyngeal carcinoma C666-1 cells, NPC43 cells and Burkitt's lymphoma Raji cells. We also show that the peptide-based probe leads to 93% growth inhibition of EBV+ tumours in mice. Our findings support the hypothesis that selective inhibition of EBNA1 dimerization can be used to afford better EBV-related cancer differentiation, and highlight the potential application of the probe as a new generation of biotracers for investigating the fundamental biological function of EBNA1 and for exploring its application as a therapeutic target.

Epstein-Barr virus (EBV) is a ubiquitous human herpes virus which causes both infectious mononucleosis and lymphoproliferative diseases^{1,2}, but the virus is well controlled by the immune system once it establishes latent infection in human hosts^{3,4}. Epstein-Barr nuclear antigen 1 (EBNA1) is the only oncoprotein expressed in all EBV-positive tumours and it plays critical roles in the maintenance, replication and transcription of the EBV genome. Furthermore, it can influence cellular gene transcription which is fundamental in the development of EBV-related tumours⁵. Given these key biological functions, EBNA1 has become an attractive target for therapeutic intervention^{6,7}. Considering that homodimerization of EBNA1 is essential for EBNA1 to function, inhibitors which can specifically prevent the dimerization process offer a novel avenue by which to target and kill EBV-positive cells^{8,9}. Several EBNA1 inhibitors have been reported to efficiently block EBNA1 homodimerization, including the small molecule, EiK1, and a short EBNA1 derived peptide (P85). EiK1 was identified *via* high-throughput screening, and it is capable of targeting the dimeric interface of EBNA1 (residues 459-607), P85 which contains a short EBNA1 derived β 3 sheet (a.a. 560-566) also targets this region (residues 560-574)⁸. However, most of the EBNA1 targeting compounds that have been reported to date cannot be easily imaged (*in vitro*) and they have low bioavailability. Both the aforementioned issues present major challenges to the field and hamper the further development of EBNA1 targeting therapeutics. To overcome the non-fluorescent nature and poor water solubility of the previously reported EBNA1 inhibitors, we recently designed a novel hybrid system, which contained a charged, water-soluble chromophore and an EBNA1-specific peptide. The charged, water-soluble chromophore-peptide bio-conjugate, **JLP₂**, enabled for the first time both simultaneous specific imaging and inhibition of EBNA1 *in vitro*⁹. However, **JLP₂** lacked specific subcellular localization and it displayed no responsive

binding which limited its further development as a tool for cellular imaging, and, as a potential selective therapeutic agent for the treatment of EBV cancers.

It is also worth noting that EBNA1 is primarily localized in the nucleus of EBV-positive cells¹⁰, and EBNA1 acts as a bridge between mitotic chromosomes and oriP-containing plasmids¹¹. One factor that has limited the success of cancer therapies is the challenging associated with specifically targeting a desired cell type¹². Despite the key role and the specific localization of EBNA1, a direct and sensitive system for visualizing EBNA1 in the nucleus and monitoring its effect on EBNA1 homodimerization is not currently available. To address this problem, we reasoned that valuable new insights and selective tumour inhibition both *in vitro* and *in vivo* could be gained if a nucleus-penetrating EBNA1-specific dual-probe could be developed. The development of responsive nucleus-specific bioprobes for *in vitro* microscopic studies of EBNA1 and selective inhibition on EBV-positive tumour has not yet been explored in detail. The work reported here offers a strategy for responsive-emission imaging in EBV-positive cells and provides highly selective and efficient *in vitro/vivo* cytotoxicity.

The rationale design (Fig. 1a) of the dual functioning probe was achieved using docking and molecular dynamic (MD) simulations and their synthesis was outlined in Sup. Fig. 1. The characterization of all intermediates and final products, including ¹H NMR, ¹³C NMR and Mass Spectra, were performed as shown in Sup. Fig. 37-48. What's more, the peptide conjugates were purified *via* HPLC, the purification and characterization was recorded in Sup. Fig. 2-6, the used solvent gradient was also recorded (Sup. Table 1 and 2). The strong interaction of **L2P4** with the wild type EBNA1 (WT-EBNA1) was confirmed by a 8.8-fold increase in its emission intensity. **L2P4** responded significantly upon binding with WT-EBNA1, and the responsive signal was found to be induced by the intermolecular charge transfer (ICT) mechanism (Fig. 2). Simultaneous

imaging and control of the growth of EBV-positive tumours have been achieved by our designed dual-function fluorescent probes through selective interference of EBNA1 homodimerization. **L2P4** displayed excellent cytotoxicity towards EBV-positive cells ($IC_{50} \sim 15 \mu M$), and minimal cytotoxicity against EBV-negative cells even at high doses (50 μM). Furthermore, **L2P4** demonstrated excellent *in vivo* toxicity against EBV-positive tumours (intra-tumour injection of 4 μg gives 92.8% growth inhibition).

Both the *in vitro* and *in vivo* studies described here demonstrated the effectiveness of **L2P4** as a dual EBV tumour-selective cancer targeting agent and responsive imaging probe. Given these findings, we envisage that **L2P4** represents an efficient tool to delineate the processes that govern EBNA1 within the nucleus. In the longer term this new level of understanding will provide exciting new opportunities for the treatment of EBV-associated tumours, such as Hodgkin lymphoma, nasopharyngeal carcinoma and a sub-group of EBV-associated stomach cancer.

Results

Rational design and MD simulations between probes and EBNA1. The X-ray crystal structure of EBNA1's DNA-binding domain (DBD) (PDB ID: 1B3T, chain A, residue 461 to 607) is α/β mixed fold comprised of 4 alpha helix and 4 beta sheet motifs which are linked by several loops (Fig. 1b and Sup. Fig. 7)¹³. Different structural motifs contribute to its distinct functional regions: the beta sheets 1-4 ($\beta 1$ - $\beta 4$) drive the formation of dimer *via* hydrophobic packing; the alpha helices 1 and 2 ($\alpha 1$, $\alpha 2$) interact with DNA *via* electrostatic interactions, while the alpha helices 3 and 4 ($\alpha 3$, $\alpha 4$) stabilize the beta sheets; the positively-charged loop 1 mediates DNA binding; and the flexible loop 5 also involves in the dimerization¹⁴.

The putative structure of EBNA1 DBD monomer was generated through the isolation from the X-ray crystal structure of its homodimer, and it was performed for a 200 ns all-atom explicit solvent MD simulations. The putative structure demonstrated a good stability and kept the original conformation during the simulation, except for the highly dynamic loop 1 and 5 which have no contribution in the homodimerization of EBNA1 (Sup. Fig. 8a, 8b). What's more, the 4 beta sheets which comprise the dimeric interface were also found to exhibit good stability (Sup. Fig. 8c). It was further evaluated for the accessibility of the dimeric interface in the putative structure, and the results suggested that the key residues (Y₅₆₁, M₅₆₃, and F₅₆₅) on the dimeric interface⁸ could be assessed by extrinsic probes (Sup. Fig. 8d). After checking the stability and accessibility of this putative structure, a representative conformation was selected out and the docking study was carried out to identify the best docked poses for each ligand-EBNA1 complex (Sup. Fig. 8e, 8f). All docked poses were then ranked using a scoring function to choose the final poses for each complex. It was found most selected poses sharing some extend similarities, for example, the interaction of the key residues in EBNA1 to YFMVF appeared in all complexes (Sup. Fig. 9).

Besides, an unexpected salt-bridging was found between the positively-charged tetrapeptide RrRK and the aspartate-rich tail in EBNA1, suggesting a second role of the NLS.

To better characterize the ligand-EBNA1 complex and calculate their binding energy, a 200 ns MD simulations were then performed using the selected docked poses. The AMBER types of the non-standard residues were parameterized (Sup. Fig. 10) and the missing force field parameters were defined (Sup. Table 3) prior to the following 200 ns MD simulations. All complexes were found to be stabilized after 50 ns, and it is hard to find a conserved binding pattern between them though sharing a same motif (YFMVF), and it is due to the affection of the salt-bridging interaction which appeared only in the ligands containing the RrRK tetrapeptide. Despite these, the main interactions suggested by MD simulations for each complex were similar (i.e. the clear hydrophobic contacts and the salt-bridging, Sup. Fig. 17). The hydrophobic interactions identified occurred between the key residues on the dimeric interface and the ligands, while the salt bridging was formed between the RrRK motif and several residues in the aspartate-rich tail in EBNA1 (D₆₀₂, D₆₀₁ and D₆₀₅). In particular, D₆₀₂ demonstrated the strongest salt bridging interaction and D₆₀₅ showed the weakest (Sup. Fig. 11-16). Taken as a whole, the MD simulations suggested two major interaction type which facilitate the binding of the designed probes to EBNA1, and they also, demonstrated a secondary role of the RrRK sequence beyond nuclei targeting (Fig. 1b).

The binding free energy for all complexes was calculated *via* Molecular Mechanics Poisson-Boltzmann Surface Area (MMPBSA) based on full trajectory. The calculated GB and PB values took the same order **L₂P₄** > **L₂P₃** > **L₂P₂** (Fig. 1c and Sup. Table 4), indicating that **L₂P₄** is likely to have the strongest binding interaction among the three probes to EBNA1.

It should be noted that an X-ray crystal structure of the EBNA1 monomer has not yet been solved and that the use of a putative one could result in errors in the numerical data generated *via* MD

simulations. In addition the rigid protein model used in the MOE-Dock approach, the implicit solvent environment in the docking experiment and an untrained scoring function for the protein-peptide case, may also introduce errors into the determination of the initial structures and thus into the subsequent MD simulations. The aforementioned points highlight that the numerical results generated in the MD simulations for the proposed protein-ligand complex structures should be viewed as indicative rather than definitive values. However, despite any potential error in the specific values calculated the overall binding trends for the ligands predicted computationally are also clearly seen experimentally (e.g. **L2P4** was validated experimentally to have the strongest binding interaction with WT-EBNA1).

Responsive emission of L₂P₄ with EBNA1. The stability of L₂P₂-L₂P₄ was performed by monitoring their emission spectrum at 37 °C during 24 hours, and all probes demonstrated a good stability in the simulated extra cellular anion mixture (PBS buffer) (Sup. Fig. 18). As discussed from the MD simulations and free energy calculations, L₂P₄ was predicted to have the strongest interaction with WT-EBNA1 of the three probes studied, and thus it potentially offered the best option by which to prevent the homodimerization of EBNA1 and ultimately inhibit the growth of EBV-positive tumour. To further assess the binding affinity of L₂P₄ to WT-EBNA1, luminescence titration experiment was carried out in PBS buffer. The results obtained from the titration experiment aligned well with the calculated data *via* MMPBSA. For example, L₂P₄ was found to have the strongest responsive signal upon the addition of WT-EBNA1 (Fig. 2a, 2b, 2c, Sup. Fig. 21), a 8.8-fold emission enhancement ($\phi_{\text{initial}} = 4\%$, $\phi_{4\mu\text{M WT-EBNA1}} = 23\%$, Sup. Fig. 19 and 20) and 25 nm emission blueshift. A 4.7 times emission enhancement was seen in the titration experiment for L₂P₃, and no emission enhancement/quenching was observed for L₂P₂ upon addition of 4 μM WT-EBNA1 (Sup. Fig. 21). The affinity strength for a probe to its binding protein can be defined as the binding constant and binding ratio. The aforementioned binding constant ($\log K_a$) was calculated for L₂P₂-L₂P₄ to WT-EBNA1 (Sup. Fig. 21). The logarithm of the fluorescence ratio demonstrated a linear relationship with that of the protein concentration. The value of $\log K_a$ was calculated to be 5.50 and 6.82 for L₂P₃ and L₂P₄ respectively, and both of the binding ratios were found to be 1:1. Considering the strongest binding of L₂P₄ to WT-EBNA1, we then further investigated the binding selectivity of L₂P₄ to WT-EBNA1 in the presence of various proteins (Fig. 2c) and biologically relevant metal ions/small molecules (Zn^{2+} , citrate etc) (Sup. Fig. 22, 23). The proteins analyzed in the selectivity assay included four EBNA1 mutant proteins and bovine serum albumin (BSA). EBNA1 mutant proteins were prepared by mutation of YFMVF to FFAVA

(yielding EBNA1-3A) or *via* conservative point mutation of Y₅₆₁, M₅₆₃, and F₅₆₅ to A (yielding EBNA1-Y₅₆₁A, EBNA1-M₅₆₃A and EBNA1-F₅₆₅A). The selectivity of **L₂P₄** for each protein was investigated by recording changes in its emission. A relatively slight emission enhancement was observed (Fig. 2c) upon addition of the four mutant EBNA1 proteins and BSA, suggesting a weaker binding of **L₂P₄** to the aforementioned proteins when compared to the results obtained in the titration experiments with WT-EBNA1 (log K_a for EBNA1-Y₅₆₁A, EBNA1-M₅₆₃A, EBNA1-F₅₆₅A and EBNA1-3A is 5.1, 3.6, 4.3, 3.9 respectively, and for BSA is 4.7).

It is well established that when an environment-sensitive fluorophore is conjugated to peptides with specific targeting, subsequent protein binding will give rise to the emission intensity and a strong blue-shift will occur due to the dramatic change in excited state dipole-moments. It is well known now that the dual fluorescence of 4-(N,N-dimethylamino)benzonitrile (DMABN) arises due to an emission from the local excited (LE) state and an “anomalous” red-shifted emission from the ICT state¹⁵⁻¹⁷. Among the numerous DMABN analogues reported to date, pyridine derivatives have been a focus of particular interest, especially in the determination of cell microviscosity¹⁸. With this in mind we proposed that a fluorescent probe consisting of an ICT state pyridine derivative fluorophore and a nucleus-permeable EBNA1-specific peptide, which generates ICT characterized emission after binding with EBNA1, could prevent the homodimerization of EBNA1, and meanwhile imaging on nucleus level in EBV-positive cells.

The absorption spectrum of **L₂P₄** was measured in various solvents (Sup. Fig. 24). The spectra showed two absorption bands at 274 nm and ~500 nm, which corresponded to the transition from ground state to LE and ICT states, respectively^{17, 19}. The maximum absorption band was slightly red-shifted in polar solvents. **L₂P₄** demonstrated dual fluorescence upon excitation, a weak but higher energy emission at 560 nm arising from the LE state and a strong emission at ~625 nm from

the ICT state were both observed (Fig. 2a, 2d, 2e). The fluorescence emission of LE band was solvent-independent, while the ICT band exhibited a marked dependence on solvent polarity, progressively blue shifted with the decreasing of solvents polarity (Fig. 2e). Besides, the emission decay of **L2P4** was measured as shown in Sup. Fig. 26 and Fig. 2f (upper, $\lambda_{\text{ex}} = 475 \text{ nm}$, monitored at 625 nm) and the emission lifetime of **L2P4** in different solvents was concluded in Sup. Table 5. The observed shorter lifetime ($\sim 0.5 \text{ ns}$) was corresponded to the LE emission, and the ICT band also demonstrated a longer lifetime (3.8 ns).

Nuclear *in vitro* imaging of L₂P₄. The *in vitro* imaging of L₂P₂, L₂P₃ and L₂P₄ in HeLa, CNE2, C666-1 and NPC43 cells were carried as shown in figure 3. HeLa is EBV-negative human cervical carcinoma cell line, CNE2 is EBV-negative nasopharyngeal carcinoma cell line, C666-1 is EBV-positive nasopharyngeal carcinoma cell line, and NPC43 is the newly derived EBV-positive nasopharyngeal carcinoma cell line which was established from a surgical resected NPC tissue from a male patient (64 years old with Stage III recurrent NPC). As previously discussed, we incorporated a NLS sequence RrRK into P₃ and P₄ to help their nucleus permeability^{20, 21}. The cellular uptake and localization of the three probes was evaluated independently using confocal imaging and flow cytometry (Fig. 3, Sup. Fig. 28, 29, 30). From these experiments, L₂P₄ was found to have a better cellular uptake compared with the other two probes in both HeLa and C666-1 cells (Sup. Fig. 28). With the significant contribution of RrRK, the subcellular localization of L₂P₃ and L₂P₄ can be observed in the nucleus of EBV-positive cells (C666-1 and NPC43 cells), whilst L₂P₂ can only be noticed in cytoplasm in the tested cells, suggesting L₂P₃ and L₂P₄ could localize on the EBV-positive cell-nucleus. In addition, two videos of L₂P₄ in HeLa and C666-1 cells were performed (Conc.: 10 µM) (Sup. Video 1 and 2). Images in the video were taken once per minute and 60 images for the first hour after drug treatment were collected to make the video. The video showed a dynamic and intuitive visual of the selective nucleus localization of L₂P₄ in EBV-positive cells.

Selective toxicity of L₂P₄ towards EBV+ cells. EBNA1 can only facilitate DNA replication of EBV by forming homodimers, thus blocking dimer formation provides a route by which to kill EBV-infected tumour cells. As is well known, the EBNA1 dimer is formed through the YFMVF-mediated interface, and this can be examined by MBS (3-maleimidobenzoyl N-hydroxysuccinimide ester, an amine-to-sulfhydryl crosslinker that contains NHS-ester and maleimide reactive groups) cross-linked dimerization assay. The MBS mediated protein crosslinking effect was represented as a ratio of dimer/monomer. The importance of YFMVF on dimerization was further investigated in the WT-EBNA1 and EBNA1 mutants (EBNA1-Y₅₆₁A, EBNA1-M₅₆₃A, EBNA1F₅₆₅A and EBNA1-3A) by its homodimerization efficiency. The results demonstrated that the dimerization efficiency was greatly decreased in EBNA1-3A, and also, a relative slight decreasing in the efficiency was observed in the other three point mutants (Sup. Fig. 27). Consistent with this observation and the luminescence titration experiment, the MBS cross-linked dimerization assay was also obviously inhibited by the designed probes as shown in Fig. 4a, 4b, 4c, 4d (P<0.001).

Considering the strong binding of L₂P₄ to WT-EBNA1 and the selective nuclear *in vitro* imaging, we sought to evaluate if L₂P₄ could deliver selective and efficient cytotoxicity towards EBV-positive cells. The MTT cytotoxicity assay of the three peptides (P₂-P₄, Sup. Fig. 31) and three peptide conjugates (L₂P₂-L₂P₄, Fig. 4e-4j) was carried out in three kinds of EBV-negative (MRC-5, HeLa and Ramos) cells and three EBV-positive (C666-1, NPC43 and Raji) cells. All probes were found to have weak cytotoxicity in EBV-negative cells even at high doses (50 µM), and they all exerted dose-dependent cytotoxicity in EBV-positive cells. Furthermore, L₂P₄ demonstrated the strongest cytotoxicity in all three EBV-positive cells. It is noteworthy that the cytotoxicity of

the three probes in EBV-positive cells was in the same order as the findings in 200 ns MD simulations, luminescence titration and *in vitro* imaging in EBV-positive cells.

Preproof

***In vivo* tumour imaging and inhibition of L₂P₄.** To further evaluate the *in vivo* performance of L₂P₄, the intra-tumoural injections of P₄/L₂P₄ in two dosage amount (2 µg Low Dosage (L) and 4 µg High Dosage (H)) in BALB/c nude mice carrying C666-1 and HeLa cell xenografts have been performed, injections were carried out biweekly with body weight and tumour measurements, mice carrying HeLa cell xenografts served as control to confirm the specific *in vivo* targeting effect of P₄/L₂P₄. Treatment with P₄/L₂P₄ on mice had no significant effects on body or organ weights when compared to control (Sup. Fig. 32, 33, 35a), indicating that neither P₄ nor L₂P₄ exhibit a toxic effect *in vivo*. C666-1 cell xenograft growth was effectively inhibited while the growth of HeLa cell xenograft was unaffected by treatment with P₄/L₂P₄ (Fig. 5d, Sup. Fig. 35b). By day 7, treatment with P₄-L, P₄-H and L₂P₄-H on C666-1 cell xenografts has led to significant decreases in tumour volume and at the end of the experiment (day 21), the average tumour volumes of mice were decrease by 65.7%, 65.5% and 92.3% (P<0.05, P<0.005 and P<0.001) respectively, when compared to control (Fig. 5d, Sup. Fig. 34). In the HeLa cell xenografts, there was no significant difference in the average tumour volume of mice treated with P₄/L₂P₄ (low or high dose) and control after 18 days (Sup. Fig. 35b). At the end of the experiment, mice were sacrificed and tumours were excised and weighed, average tumour weights were decreased on C666-1 cell xenografts after treatment with P₄-L, P₄-H and L₂P₄-H by 72.6%, 86.6% and 92.8% (NS, P<0.05 and P<0.005) respectively, when compared to control (Fig. 5a, 5b, 5c and 5e). While in the HeLa cell xenografts, there was no obvious difference in the average tumour weights (Sup. Fig. 35c, 36). The significant and selective inhibition of P₄/L₂P₄ on EBV-positive tumour confirmed their EBV-targeting specificity and indicated the conjugation of L₂ to P₄ does not affect its tumour inhibitory effect.

Furthermore, the fluorescence imaging of the excised C666-1 tumours confirmed the fluorescence from **L₂P₄** treated tumours (Fig. 5f), indicating the presence of signal 48 hours post-intra-tumoural injection. As expected, no fluorescent signal was detected in control or **P₄** treated tumours.

Proof

Discussion

Our initial MD studies suggested that a network of hydrophobic interactions and salt bridging mediates the binding of **L2P4** to the dimeric interface of EBNA1 (Fig. 1). The selective and strong binding of **L2P4** to EBNA1 was further confirmed using luminescence titration experiment (Fig. 2). **L2P4** was found to localise in the nucleus of EBV-positive cells, but not that of EBV-negative cells. The observed selective emission of **L2P4** on nucleus was generated by its binding with EBNA1 (Fig. 3).

Our study also revealed that EBNA1 mutants (especially EBNA1-3A) were not able to undergo homodimerization (Sup. Fig. 27), emphasizing the importance of the dimeric interface (YFMVF) on EBNA1 dimer formation. The analysis of the WT-EBNA1 dimerization efficiency upon addition of the designed probes using a MBS cross-linked dimerization assay showed that the probes can significantly interfere with EBNA1 dimer formation (Fig. 4a, 4b, 4c, 4d). Extensive cytotoxicity assays performed against both EBV positive and negative cells demonstrated the significant and selective inhibition of **L2P4** on EBV-positive cells, more importantly, revealed the reason for the selective cytotoxicity is the inhibition on EBNA1 dimerization process (Fig. 4e-4j). Finally, studies of **L2P4** on mice carrying C666-1 and HeLa cell xenografts confirm that it has EBV-targeting specificity and indicated that our designed probe can be successfully applied to target and inhibit the growth of EBV-positive tumours *in vivo* (Fig. 5).

Our data clearly demonstrates that **L2P4** can selectively inhibit EBV-positive tumours-both *in vitro* and *in vivo*, and that it does this *via* interfering with EBNA1 homodimerization. We are confident that our present work will revive research interest and open new doors in the study of EBNA1 inhibition by shining light onto previously unknown areas – visualization of the binding of probe with EBNA1 and the dimerization inhibition process on EBV-positive cell nucleus, with **L2P4** as a solid foundation for further development against EBV-related malignancies with emphasis put on EBNA1-related factors such as Zn^{2+} , followed by realization of these probes in *in vitro* and *in vivo* imaging applications.

Methods

Molecular dynamics simulation. All the simulations reported herein were performed with the unbiased MD program in Amber 14. The ff99SBildn force field²² has been used to describe all molecular systems. For each of the simulations, the peptide was solvated in a periodic truncated cubic box with TIP3²³ water molecules, providing 10 Å buffer distance between the peptide surface and the periodic box edge. The peptide was then heated from 100 K to 300 K in 20 ps. The system was further equilibrated in 200 ps with constant pressure and temperature (NPT) before starting the 200 ns NPT production simulation. A 2 fs time step and SHAKE-enabled setting were applied during the equilibration and production stages, and Berendsen thermostat was used for temperature controlling. Detailed MD simulations of peptides/probe-EBNA1 complexes can be found in Supplementary Materials.

Luminescence titration analysis. The measurement of the binding constant and selectivity of the designed probes was performed by luminescence titration analysis. It was conducted with gradually addition of various analytes (e.g. WT-EBNA1, EBNA1 mutants, BSA and metal ions), which will be ceased either when the volume of added analytes totalled 5% of the probes or the influence on luminescence was saturated.

Protein samples preparation. Five protein samples were used during this work. WT-EBNA1 protein (379-641 a.a.) fused with glutathione S-transferase was expressed in *Escherichia coli* and purified by glutathione sepharose 4B rinse (GE Healthcare Dharmacon), afterwards 5 µg EBNA1 was prepared and incubated with MBS at 37°C for 10 minutes. The protein was separated on an SDS-PAGE gel, transferred onto the nitrocellulose membrane and blotted by antibodies (#RG001040, Solarbio, Bioscience & Technology Co., LTD). EBNA1 mutant proteins were prepared by mutation of YFMVF to FFAVA (yielding EBNA1-3A mutant) or conservative point mutation of Y₅₆₁, M₅₆₃, F₅₆₅ to A (yielding EBNA1-Y₅₆₁A, EBNA1-M₅₆₃A and EBNA1-F₅₆₅A) through site-directed mutagenesis.

Cell culture. The EBV-negative MRC-5 and HeLa cells were provided by the Shanghai cell bank, Chinese Academy of sciences; the EBV-negative nasopharyngeal carcinoma CNE2 and EBV-positive nasopharyngeal carcinoma C666-1 cells were supplied by the Hong Kong NPC AoE Cell Line Repository; the EBV-negative

Burkitt's lymphoma Ramos and EBV-positive Burkitt's lymphoma Raji cells were afforded by H. L. Lung; the newly derived EBV-positive nasopharyngeal carcinoma NPC43 cells were contributed by S. W. Tsao.

MRC-5 (normal lung fibroblasts) cells were grown in Minimum Essential Medium (MEM); HeLa (cervical carcinoma) cells were grown in Dulbecco's Modified Eagle Medium (DMEM); CNE2 and C666-1 (nasopharyngeal carcinoma), Ramos and Raji (Burkitt's lymphoma) cells were grown in Roswell Park Memorial Institute (RPMI)-1640 medium. All medium used was supplemented with 10% fetal bovine serum (FBS), 1% penicillin and streptomycin at 37°C and 5% CO₂. NPC43 cells were maintained in RPMI1640 with 10% serum and 4 µM ROCK inhibitor Y27632 ROCK (Enzo Life Sciences).

NPC43 cells were established from a surgical resected NPC tissue from a male patient, 64 years old with Stage III recurrent NPC. The NPC43 cell harbour EBV virus and was kept in RPMI supplemented with 10% FBS and 4 µM of a Rho kinase inhibitor, Y27632 over 200 population doublings. The NPC43 is tumourigenic when injected at subcutaneous site (10 million cells) of NOD/SCID mice. STR profiling confirms its origin from the NPC patients. The NPC43 cells could be induced to under lytic reactivation of EBV by treatment with TPA/sodium butyrate and infectious EBV could be harvested from supernatant of NPC43 cells. All cell line used in the current study were tested and confirmed to be mycoplasma-negative, and authenticated by using the AmpF ℓ STR Identifier PCR Amplification kit (Life Technologies).

Flow cytometry analysis. HeLa and C666-1 cells (10⁵ per sample) were seeded to 35 m Petri dishes overnight. Afterwards, the cells were incubated with the probes as indicated, and then washed with PBS several times. Cellular uptake was evaluated with flow cytometry under 488 nm excitation generated by an argon laser. The emission was obtained by using FL2-H (log). 10000 events were analyzed to get the cellular uptake.

***In vitro* imaging and Co-staining.** Cells were incubated for 6 hours before monitoring/imaging. For co-staining experiments after incubation cells were further treated with 1nM nucleus lyso Green DND-26 tracker/mito Green FM M7514 tracker/Hoechst 33342 nuclear dye for 1 hour. Imaging was conducted with a commercial multi-photon Leica SP8 confocal microscope equipped with a coherent fs laser (680 nm to 1050 nm), argon laser (432

nm, 457 nm and 488 nm), He-Ne laser (632 nm), UV-lamp and controlled CO₂ content stage-top tissue culture chamber (2-7 % CO₂, 37°C).

Cytotoxicity test. The MTT viability assay was performed according to standard methods. In brief, cells (3×10^3 /well) were seeded in 96-well plates 24 hours prior to exposure to the probes. The cells were incubated with the probes in the dark for another 24 hours. The cytotoxicity was determined by the MTT reduction assay. The cell monolayers were rinsed with phosphate-buffered saline (PBS) and then incubated with 50 uL MTT [3-(4,5-dimethylthiazol-2-yl)-2,5-diphenyltetrazolium bromide] solution (0.5 mg/ mL) at 37°C for 3 hours. Then the media were removed, and 100 uL of DMSO solubilizing reagent was added and shaken for 30 minutes to dissolve the formed formazan crystals in the living cells.

Nude mice carrying C666-1/HeLa xenograft and intra-tumoural injection (HeLa xenografts served as control). C666-1/HeLa cells (1×10^7) were suspended in serum free medium (C666-1) or mixed 1:1 with Matrigel (HeLa) to a final volume of 150µl and injected into the right flanks of male (C666-1) or female (HeLa) 6- to 8-week-old BALB/c nude mice, which were all obtained from BioLASCO (Taiwan). When tumours grew to an average volume of 200–300 mm³, prior to initiation of treatment, xenografted mice were randomized into groups (for grouping refer to Supplementary tables 6 & 7) based on tumour size (i.e. no individual mouse demonstrated more than 10% difference in tumour size group counterparts) and ANOVA performed to ensure that there were no statistical differences between groups. **P4** and **L2P4** in 0.1% DMSO at the desired dose (2 or 4 µg/tumour; low or high dose) were injected directly into the tumour using a 29 gauge syringe. Mice receiving an equivalent volume of 0.1% DMSO alone served as controls. Body weight and tumour volumes were measured twice weekly. Tumour volumes were calculated as $(\text{length} \times \text{width}^2)/2$. Intra-tumoural tumour injections were repeated twice weekly, after which the mice were sacrificed and their tumours harvested and weighed. Investigators were blind to the treatment groups during the experiments and data analysis. All animals were included in the analysis, no power analyses were used to calculate the sample size for the animal studies. All animals experiments were approved by the Department of Health of the Hong Kong Government, Hong Kong Baptist University Committee

on the Use of Human and Animal Subjects in Teaching and Research and the Animal Subjects Ethics Subcommittee of Hong Kong Polytechnic University.

Statistical analysis. The intensity of the protein bands and raw images were measured by Gel-Pro Analyzer to obtain the average of three independent experiments, showed as mean \pm S.D. The results were presented as the column plot operated by GraphPad Prism 5.0. Single factor analysis of variance was used to detect the significance of difference. The absorbance of the formed formazan crystals in cytotoxicity test was measured at dual wavelength, 540nm and 690nm, on a Labsystem Multiskan microplate reader (Merck Eurolab, Switzerland). Each dosed concentration was performed in triplicate wells, and repeated twice for the MTT assay. Data were shown as mean \pm S.D. Statistical analyses of tumour size and volume in the animal studies were conducted using the Student's t-test. Results of $P < 0.05$ were considered significant. Data were expressed as mean \pm SEM.

Data availability

The authors declare that all data supporting the findings of this study are available within the paper and its supplementary information. In addition underlying research data for this paper is also available in accordance with the EPSRC open data policy from DOI: 10.15128/r2v692t620b.

References

1. Cohen, J. I. Epstein-Barr virus infection. *N. Eng. J. Med.* **343**, 481-492 (2000).
2. Young, L. S. & Rickinson, A. B. Epstein-Barr virus: 40 years on. *Nat. Rev. Cancer* **4**, 757-768 (2004).
3. Thorley-Lawson, D. A. Epstein-Barr virus: exploiting the immune system. *Nat. Rev. Immunol.* **1**, 75-82 (2001).
4. Paludan S. R., Bowie A. G., Horan K. A. & Fitzgerald K. A. Recognition of herpesviruses by the innate immune system. *Nat. Rev. Immunol.* **11**, 143-154 (2011).
5. Wood V. H. J. *et al.* Epstein-Barr virus-encoded EBNA1 regulates cellular gene transcription and modulates the STAT1 and TGF β signalling pathways. *Oncogene* **26**, 4135-4147 (2007).
6. Frappier L. The Epstein-Barr virus EBNA1 protein. *Scientifica* **2012**, 438204 (2012).
7. Li, N., Thompson, S., Jiang, H., Liberman, P. M. & Luo, C. Development of drugs for Epstein-Barr virus using high-throughput *in silico* virtual screening. *Expert. Opin. Drug Discov.* **5**, 1189-1203 (2010).
8. Sun, Y. K. *et al.* Small molecule and peptide-mediate inhibition of Epstein-Barr virus nuclear antigen 1 dimerization. *Biochem. Biophys. Res. Commun.* **424**, 251-256 (2012).
9. Jiang, L. *et al.* EBNA1-specific luminescent small molecules for the imaging and inhibition of latent EBV-infected tumor cells. *Chem. Commun.* **50**, 6517-6519 (2014).
10. Fisher, N., Vo, M. D., Mueller-Lantzsch N. & Grässer, F. A. A potential NES of the Epstein-Barr virus nuclear antigen 1 (EBNA1) does not confer shuttling. *FEBS. Lett.* **447**, 311-314 (1999).
11. Kanda, T., Otter, M. & Wahl, G. M. Coupling of mitotic chromosome tethering and replication competence in Epstein-Barr virus-based plasmids. *Mol. Cell. Biol.* **21**, 3576-3588 (2001).
12. Vacik J., Dean B. S., Zimmer W. E. & Dean D. A. Cell-specific nuclear import of plasmid DNA. *Gene ther.* **6**, 1006-1014 (1999).
13. Bochkarev, A., Bochkareva, E., Frappier, L. & Edwards, A. M. The 2.2 Å structure of a permanganate-sensitive DNA site bound by the Epstein-Barr virus origin binding protein, EBNA1. *J. Mol. Biol.* **284**, 1273-1278 (1998).

14. Correia, B. *et al.* Crystal structure of the gamma-2 herpesvirus LANA DNA binding domain identifies charged surface residues which impact viral latency. *PLoS Pathog.* **9**, e1003673 (2013).
15. Lippert, E. *et al.* Umwandlung von elektronenanregungsenergie. *Angew. Chem.* **73**, 695-706 (1961).
16. Grabowski, Z. R. & Rotkiewicz, K. Structural changes accompanying intramolecular electron transfer: Focus on twisted intramolecular charge-transfer states and structures. *Chem. Rev.* **103**, 3899-4031(2003).
17. Sahoo, D. & Chakravorti, S. Dye-surfactant interaction: modulation of photophysics of an ionic styryl dye. *Photochem. Photobiol.* **85**, 1103-1109 (2009).
18. Wandelt, B., Mielniczak, A., Turkewitsch, P., Darling, G. D. & Stranix, B. R. Substituted 4-[4-(dimethylamino)styryl] pyridinium salt as a fluorescent probe for cell microviscosity. *Biosens. Bioelectron.* **18**, 465-471 (2003).
19. Chakraborty, A., Kar, S. & Guchhait, N. Secondary amino group as charge donor for the excited state intramolecular charge transfer reaction in trans-3-(4-monomethylamino-phenyl)-acrylic acid: Spectroscopic measurement and theoretical calculations. *J. Photochem. Photobiol. A: Chem.* **181**, 246-256 (2006).
20. Mahon, K. P. *et al.* Deconvolution of the cellular oxidative stress response with organelle-specific peptide conjugates. *Chem. Biol.* **14**, 923-930 (2007).
21. Puckett, C. A. & Barton, J. K. Targeting a ruthenium complex to the nucleus with short peptides. *Bioorg. Med. Chem.* **18**, 3564-3569 (2010).
22. Lindorff-Larsen, K. *et al.* Improved side-chain torsion potentials for the amber ff99SB protein. *Proteins* **78**, 1950-1958 (2010).
23. Jorgensen, W. L., Chandrasekhar, J., Madura, J. D., Impey, R. W. & Klein M. L. Comparison of simple potential functions for simulating liquid water. *J. Chem. Phys.* **79**, 926 (1983).

Acknowledgements

This work is funded by the Hong Kong Baptist University (FRG2/14-15/013013), Hong Kong Polytechnic University (HKPolyU), Hong Kong Research Grants Council (HKBU 20301615), Hong Kong Polytechnic University Central Research Grant (G-UC08), Hong Kong Research Grants Council (PolyU 153012/15P), University Research Facility for Chemical and Environmental Analysis (UCEA) and Area of Excellent Grants (1-ZVGG) of Hong Kong Polytechnic University, HKBU and HKPolyU Joint Research Programme (RC-ICRS/15-16/02F-WKL02F-WKL), the Engineering and Physical Sciences Research Council (EPSRC, Durham University, DTA award) and Research Grants Council of the HKSAR for the NPC Area of Excellence (AoE/M 06/08 Center for Nasopharyngeal Carcinoma Research).

Author contributions

N.-K. M. and K.-L. W. conceived and supervised the project. L. J. performed the synthesis, characterization, spectroscopic properties measurement and cytotoxicity assay in normal and some EBV-negative cells; H. L. contributed the photophysical data analysis. R. L. purified the WT-EBNA1 and EBNA1 mutants, and conducted the dimerization assay; T. H., Z.-X. B. and W.-T. W. contributed the MD simulation; C.-F. C. carried out the confocal imaging, co-localization and some cytotoxicity assay; S. L., J. Z. and S. L. C. performed the peptides synthesis, and purified the peptide conjugates; W.-Y. W., M. M.-L. L., B. D. Chan and W. C. S. T. carried out the *in vivo* inhibition. M. L. L., H. L. L., S. W. T. and G. T. contributed the *in vitro* cytotoxicity in EBV positive and negative pairs cancer cell lines; G.-L. L. in cell work and molecular design; L. J., W.-L. C., W.-S. L., S. L. C., and K.-L. W. wrote the manuscript.

Competing financial interests

The authors declare no competing financial interests.

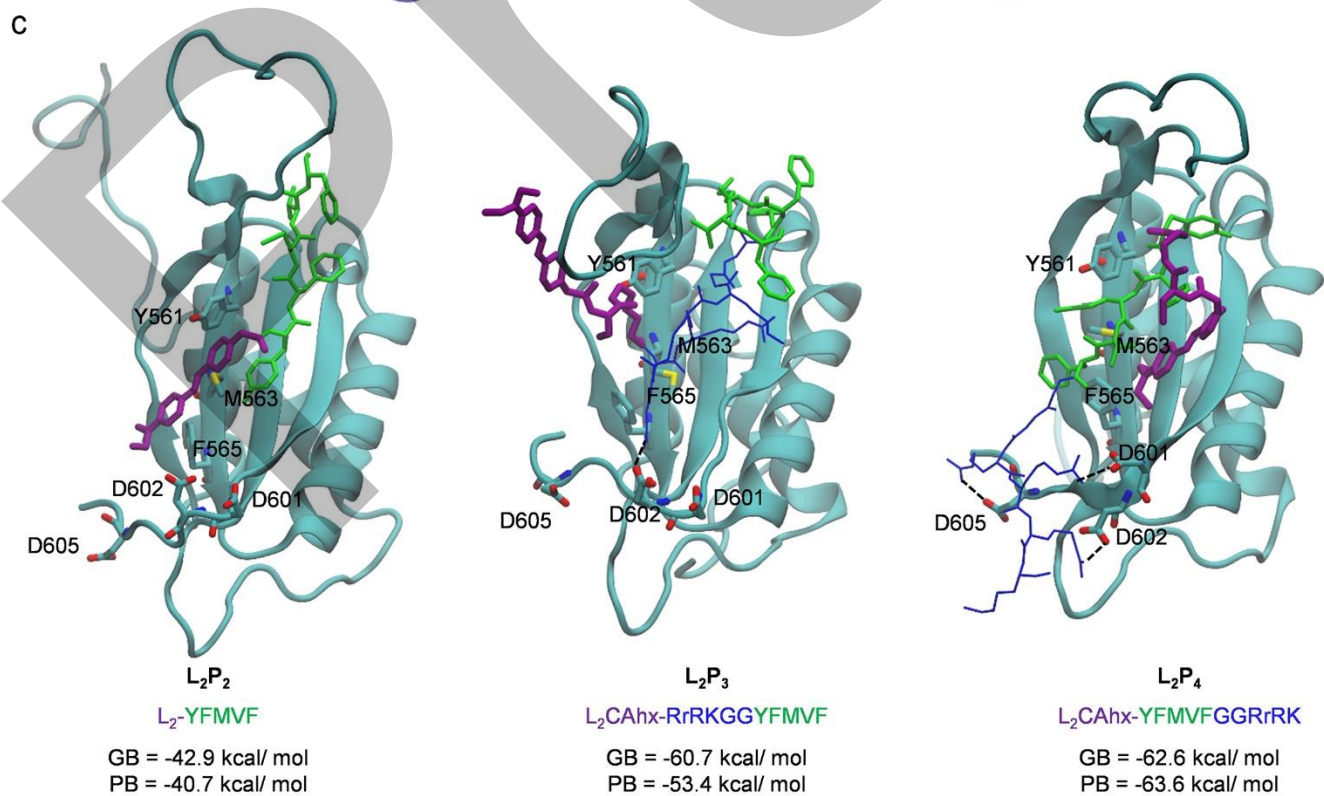
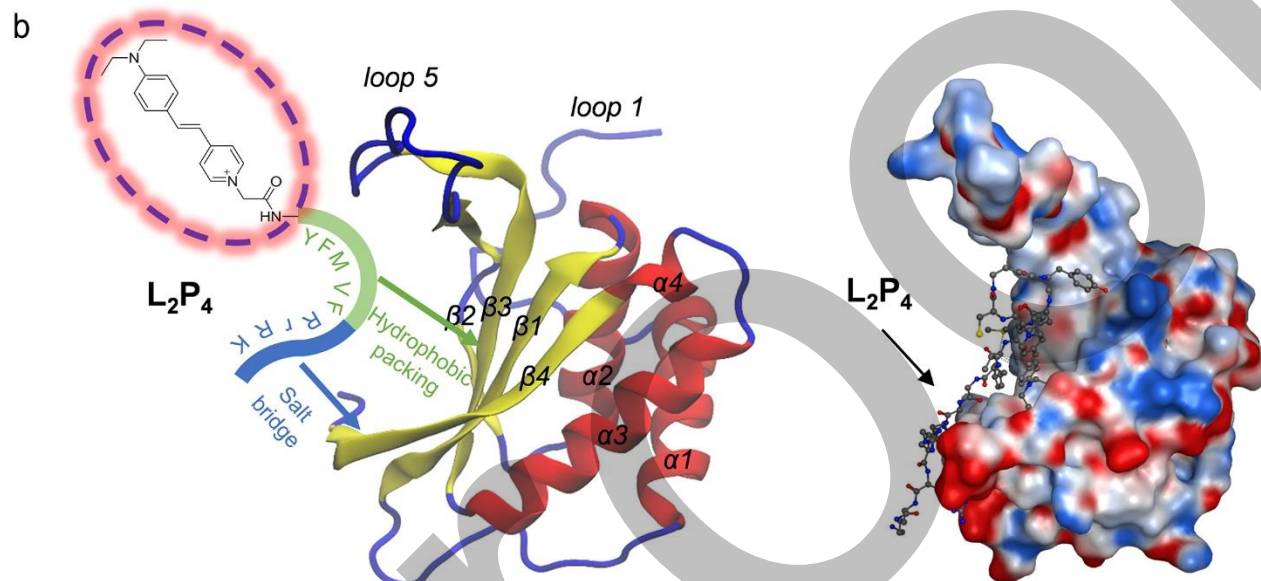
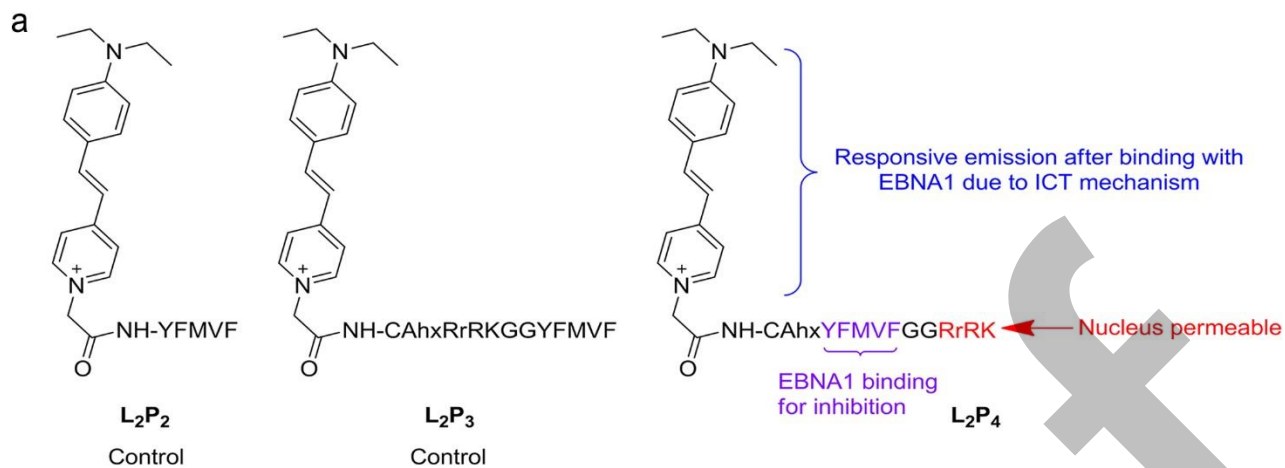


Figure 1. The rational design of the probes and the MD simulations of the designed probes to EBNA1.

(a) The chemical structures of the designed probes (**L₂P₂**, **L₂P₃** and **L₂P₄**). **P₂** is an EBNA1-specific peptide which is derived from β 4 of EBNA1, while **P₃** and **P₄** are EBNA1-specific and nucleus-penetrating peptides which also contain an RrRK motif in the middle (**P₃**) or at the C-terminus (**P₄**) of the sequence. The fluorescent group is always located at the N-terminus of **P₂**, **P₃** and **P₄**; (b) The suggested interactions between **L₂P₄** and the putative monomer structure of EBNA1 DBD domain by rendering EBNA1 in ribbons (left) or electrostatic surface (right) from MD simulation. The putative structure is generated through the isolation of the X-ray crystal structure of EBNA1-DNA complex (PDB ID: 1B3T). It's suggested that the designed probes will bind to the EBNA1 dimeric interface primarily *via* hydrophobic interactions with the YFMVF motif, and that such interactions can be enhanced by further electrostatic interactions with the RrRK motif; (c) The representative conformations of the designed probes and EBNA1 in the MD simulation. The calculated GB and PB values represented the binding free energy between the designed probes and EBNA1 (GB, Generalized Born, PB, Poisson Boltzmann).

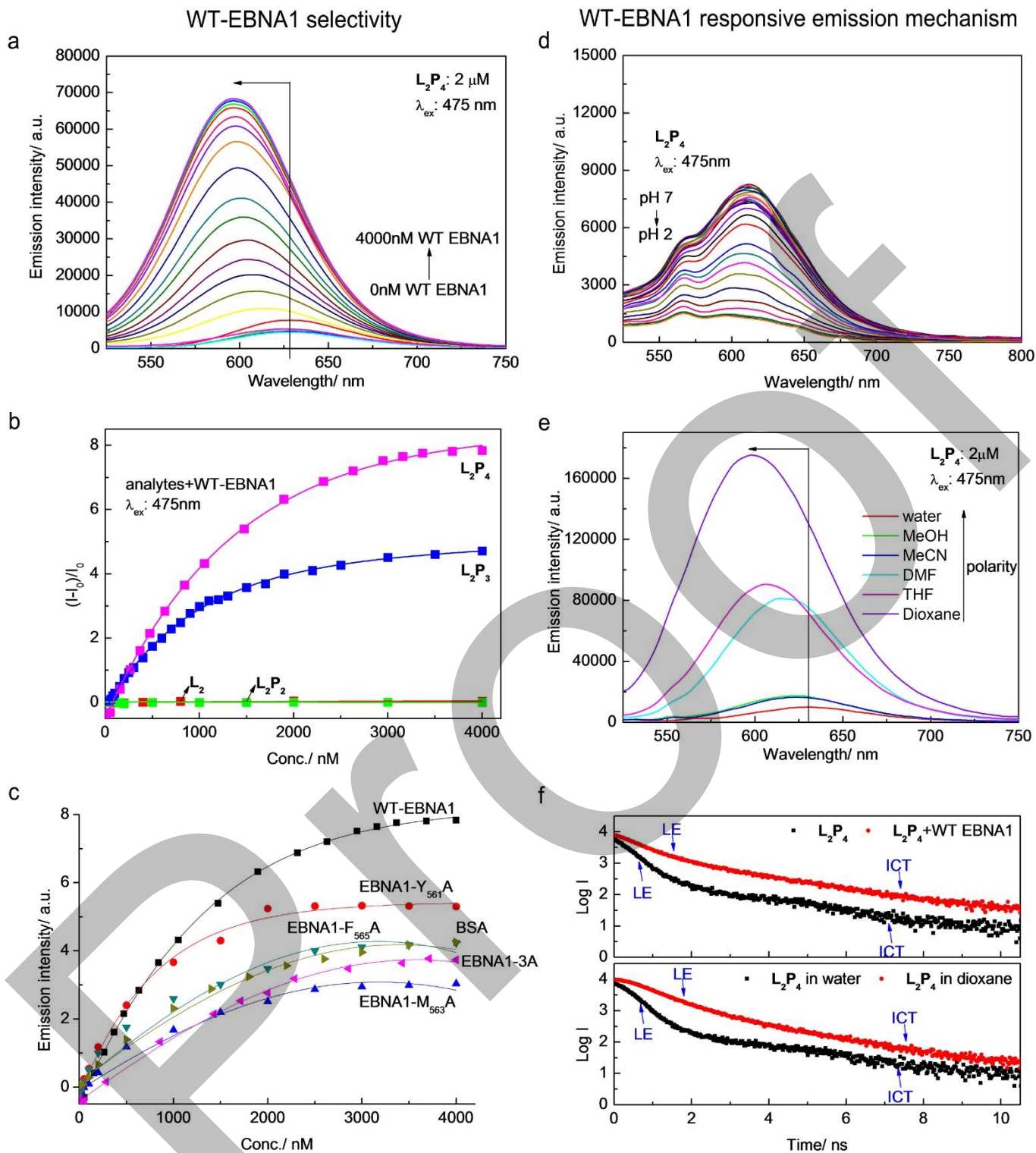


Figure 2. The selective and responsive signal of L_2P_4 upon addition of EBNA1. (a) The emission spectra of L_2P_4 with 8.8-fold responsive emission enhancement and 25 nm blueshift upon addition with WT-EBNA1; (b) The emission intensity change of L_2 , L_2P_2 , L_2P_3 and L_2P_4 upon addition with WT-EBNA1; (c) The selectivity assay of L_2P_4 in the presence of various proteins; (d) The emission spectra of L_2P_4 in various pH buffer solution, for

the confirmation of ICT state and determination of pK_a value (The case of **L₂P₃** was shown in Sup. Fig. 25). The emission band gradually decreased as the pH was lowered from 7 to 2. This finding is consistent with the characteristic of an ICT emission, which is the ICT state emission decreases at lower pHs because the nitrogen atoms become protonated in lower pHs and its lone pair is not available to generate an ICT excited state; (e) The emission spectra of **L₂P₄** in solvatochromism study with increasing solvent polarity; (f) Emission lifetime decay of **L₂P₄** upon binding with WT-EBNA1 (upper) and solvatochromism (lower) with increasing solvent polarity ($\lambda_{ex} = 475$ nm). Comparatively large LE emission decay and corresponding smaller ICT decay was found in less polar solvents, indicating a smaller dipole moment and consequently an upshift of the ICT state. Additionally, the emission lifetime of **L₂P₄** upon binding with WT-EBNA1 was found similar to that in polar solvents.

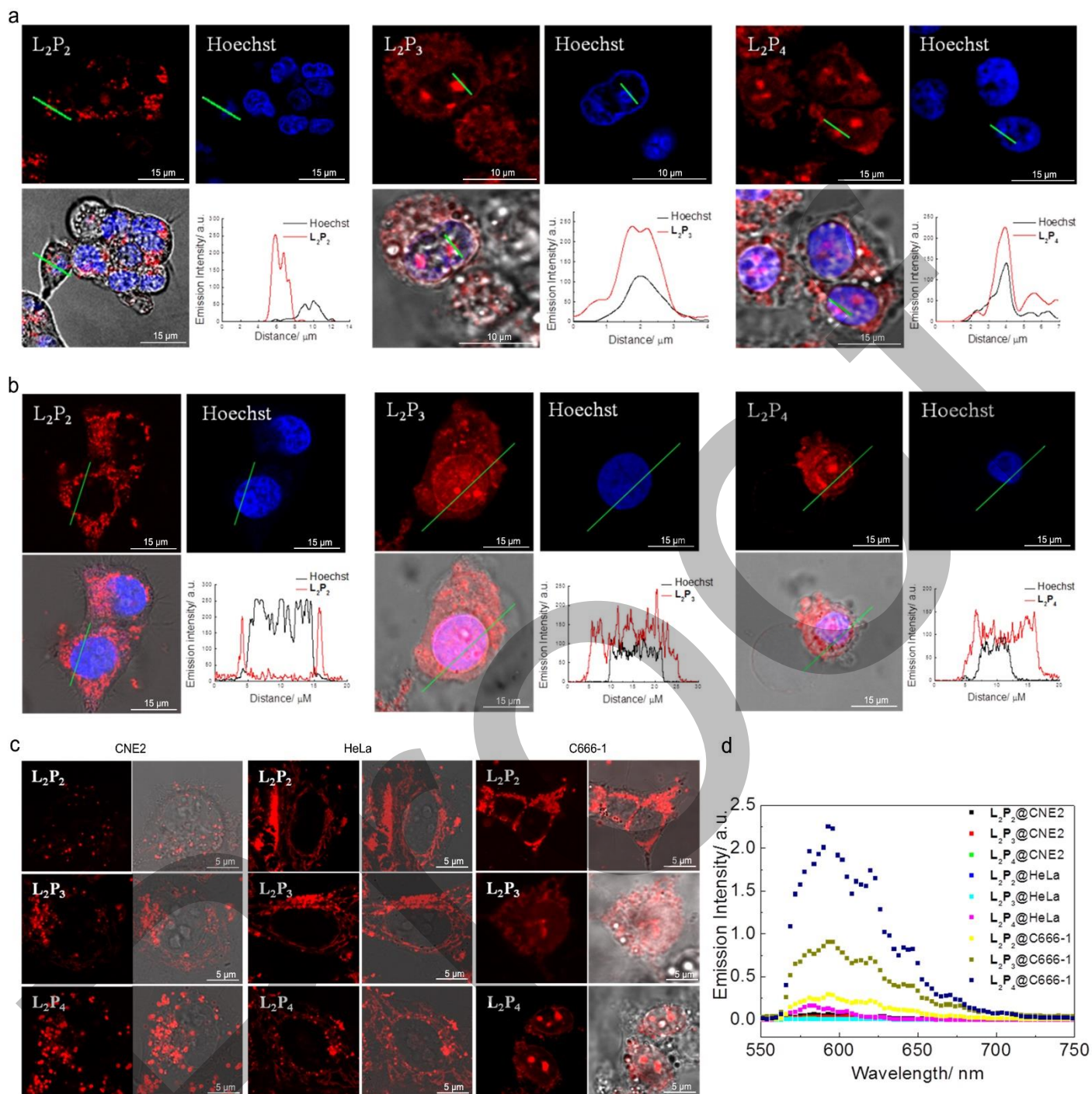


Figure 3. *In vitro* imaging of the designed probes in EBV- positive and negative cells. **(a)** *In vitro* imaging of L_2P_2 , L_2P_3 and L_2P_4 in EBV-positive nasopharyngeal carcinoma C666-1 cells. **(b)** *In vitro* imaging of L_2P_2 , L_2P_3 and L_2P_4 in newly derived EBV-positive nasopharyngeal carcinoma NPC43 cells ($\lambda_{\text{ex}} = 488 \text{ nm}$, $\lambda_{\text{em}} = 500\text{-}650 \text{ nm}$, Filter = BP500). C666-1 and NPC43 cells were treated with L_2P_2 , L_2P_3 or L_2P_4 (10 μM) for 6 hours, and then co-stained with nuclear dye Hoechst 33342 (1 nM) for 1 hour. Profiles of the emission intensity of the probes and

Hoechst 33342 were plotted along the green line, the shape and location of the emission band from **L₂P₄** found in the nucleus (by lambda scan) was similar to the data obtained in the solution under the same excitation. (c) *In vitro* imaging of **L₂P₂**, **L₂P₃** and **L₂P₄** in EBV-negative (CNE2 and HeLa) and EBV-positive C666-1 cells. The emission of **L₂P₄** was found to be selective in EBV-positive cells over EBV-negative cells. (d) *In vitro* emission spectra of **L₂P₂**, **L₂P₃** and **L₂P₄** in cell nucleus under the confocal microscope (Leica SP8). **L₂P₄** showed three times stronger emission than **L₂P₃** in the EBV-positive C666-1 cells. Scale bars were shown in the figure.

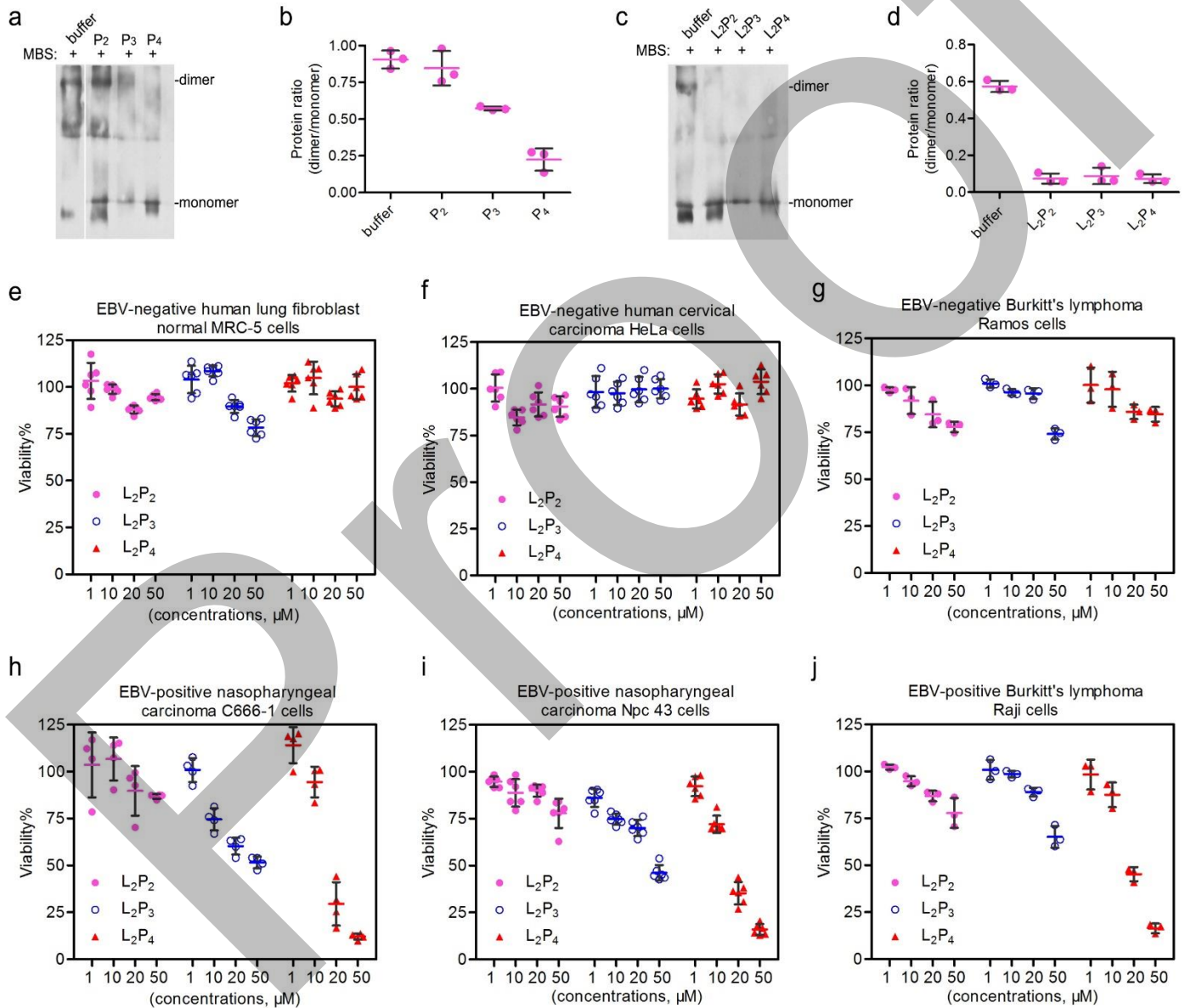


Figure 4. a-d EBNA1 homodimerization assay. WT-EBNA1 were subjected to MBS cross-linked dimerization assay upon addition of peptides (**P₂-P₄**, a and b) and peptide conjugates (**L₂P₂-L₂P₄**, c and d). The inhibitory

efficiency was measured by determining the protein ratio of EBNA1 dimer/ monomer (**b** and **d**), the intensity of each protein bands were measured by obtaining the average of three independent experiments, showed as mean \pm S.D. **e-j** Cytotoxicity assay. Cytotoxicity of **L₂P₂-L₂P₄** on EBV-negative (**e**) human lung fibroblast normal MRC-5, (**f**) human cervical carcinoma HeLa, (**g**) Burkitt's lymphoma Ramos cell lines and EBV-positive (**h**) nasopharyngeal carcinoma C666-1, (**i**) newly-derived nasopharyngeal carcinoma NPC43, (**j**) Burkitt's lymphoma Raji cell lines were assayed. Each dosed concentration was performed in triplicate wells, and repeated twice for the MTT assay. Data were shown as \pm S.D. (incubation time: 24 hours).

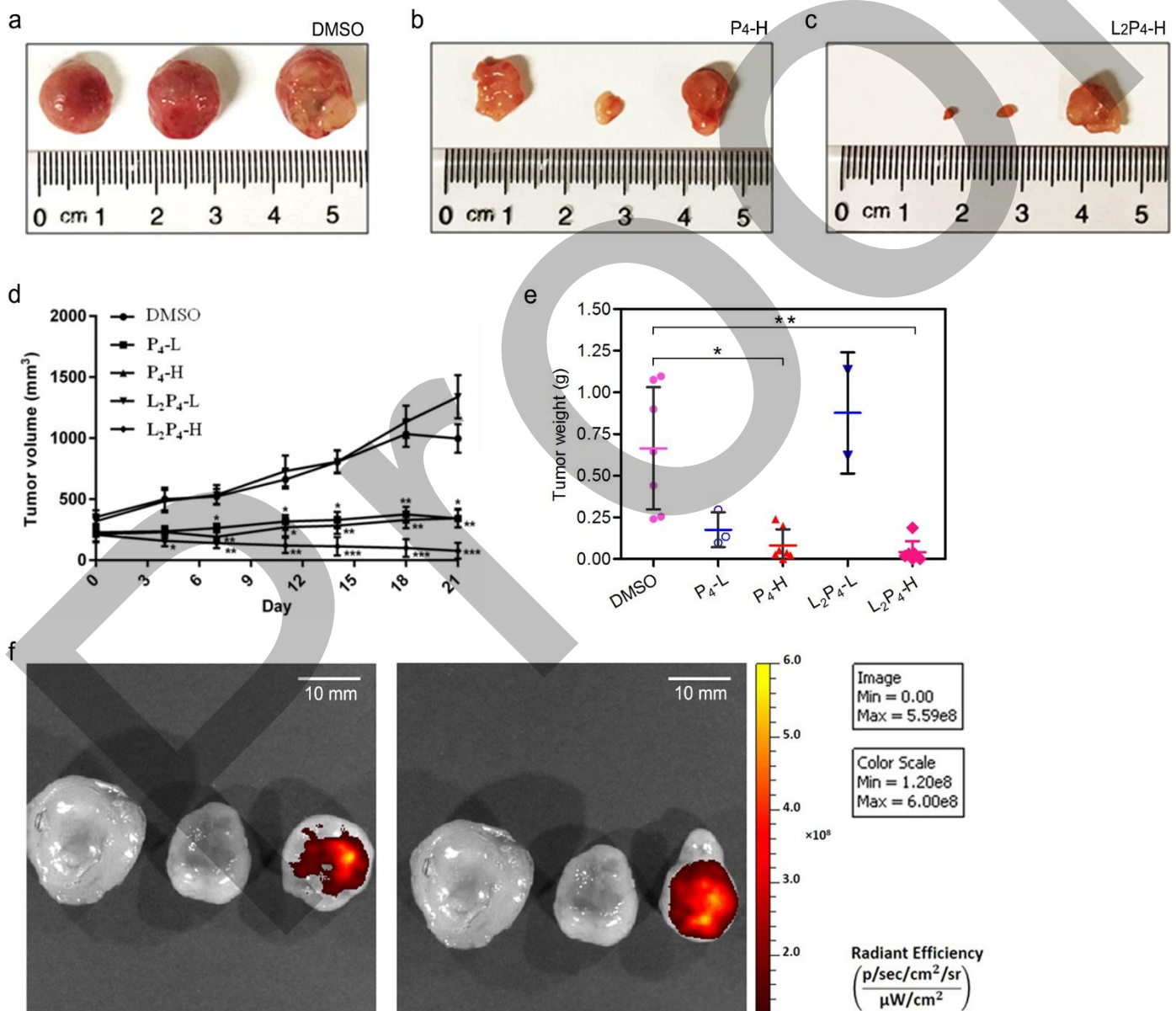


Figure 5. *In vivo* toxicity studies of **P₄** and **L₂P₄** (4 μ g/ tumour) as EBV-specific anti-cancer agents. (**a-e**) *In vivo*

tumour inhibition assays of **P4** and **L2P4**; Mice were treated with intra-tumoural injections of **P4**, **L2P4** or DMSO (vehicle) twice-weekly for 21 days. At the experimental endpoint, tumours were excised, weighed and photographed (a) Control (vehicle); (b) **P4**; (c) **L2P4** (d) tumour volume and (e) tumour weight. Average tumour volume and weights from each group in mm³ and grams respectively (for grouping and measurement numbers refer to Sup. Table 6). Data were expressed as mean \pm SEM, *, $p < 0.05$, **, $p < 0.005$, ***, $p < 0.001$. (f) Representative *ex vivo* fluorescence images of excised C666-1 tumours. Tumours were excised upon mouse sacrifice and fluorescence intensity was detected using the IVIS Lumina system 48h after intra-tumoural injection at 460 nm excitation/ 520 nm emission. Fluorescent signals were quantified as total radiant efficiency ([photons/s/cm²/sr]/[μ W/cm²]). Scale bars were shown in the figure.